

ABounD: Adversarial Boundary-Driven Few-Shot Learning for Multi-Class Anomaly Detection

Runzhi Deng¹ Yundi Hu¹ Xinshuang Zhang¹ Zhao Wang² Xixi Liu²
 Wang-Zhou Dai¹ Caifeng Shan¹ Fang Zhao^{1†}

¹School of Intelligence Science and Technology, Nanjing University, Suzhou, Jiangsu, China

²China Mobile Zijin Innovation Institute, Nanjing, Jiangsu, China

{rzdeng, huyd}@smail.nju.edu.cn

Abstract

*Few-shot multi-class industrial anomaly detection remains a challenging task. Vision-language models need to be both category-adaptive and sharply discriminative, yet data scarcity often blurs the boundary between normal and abnormal states. This ambiguity leads to missed subtle defects and the rejection of atypical normal samples. We propose **ABounD**, an Adversarial **Boundary-Driven** few-shot learning for multi-class anomaly detection, which is a unified learning framework that integrates semantic concept learning with decision boundary shaping. The **Dynamic Concept Fusion (DCF)** module produces class-adaptive prompts by fusing generalizable priors with class-specific cues, conditioned on image features. Meanwhile, **Adversarial Boundary Forging (ABF)** sculpts a more precise decision margin by generating boundary-level fence features via PGD-style perturbations. Training is conducted in a single stage under a Concept-Boundary Loss, where ABF provides the main supervisory signal and semantic-spatial regularizers stabilize the optimization. This synergy yields a decision boundary that closely follows normal data while preserving flexibility and robust semantic alignment. Experiments on MVTec-AD and VisA datasets demonstrate state-of-the-art performance in the task of few-shot multi-class anomaly detection.*

1. Introduction

Visual anomaly detection plays a vital role in industrial quality control. A crucial yet challenging setting is *few-shot multi-class anomaly detection* [21], where the goal is to detect defects across multiple product categories using only a few normal samples per class. This setting mirrors real manufacturing scenarios, where anomalies are infrequent and data collection is costly, making reliable generalization under limited supervision particularly difficult.

Vision-Language Models (VLMs), notably CLIP [16], offer a promising route by aligning images with natural-language concepts (e.g., “flawless”, “damaged”). By leveraging large-scale image-text pretraining, Recent approaches such as WinCLIP [7], PromptAD [9], AnomalyCLIP [25] and One-for-All [12] show that textual priors can boost few-shot anomaly detection.

However, a fundamental challenge remains: the learned representations must be both *adaptive* to intra-class variations and *discriminative* against subtle anomalies. Adaptiveness requires that the feature space for normal samples be inclusive, while discrimination demands a sharp and precise decision boundary. Prior methods [9, 12, 26] often struggle to balance this trade-off. As illustrated in Fig. 1(a, b), original CLIP tends to form a loose margin, while many few-shot methods either over-tighten the boundary, rejecting atypical-but-normal instances, or produce ambiguous margins that overlook fine-grained anomalies, resulting in unstable decisions near the true normal manifold.

To address this challenge, we propose **ABounD**, an Adversarial **Boundary-Driven** few-shot learning for multi-class anomaly detection, which is a unified learning framework that couples semantic concept learning with decision-boundary shaping (Fig. 1c). First, **Dynamic Concept Fusion (DCF)** generates class-adaptive prompts by combining generalizable Mixture-of-Experts semantics with learnable class-specific cues, conditioned on the image’s global features. Second, **Adversarial Boundary Forging (ABF)** explicitly sculpts the margin by generating *fence features* via PGD-based perturbations [14], guided by balance and dispersion objectives that place diverse hard examples near the decision frontier. Unlike prior decoupled or stage-wise pipelines [13, 19, 28], ABounD optimizes both modules *in a single stage* under a *Concept-Boundary Loss (CBL)*, where ABF serves as the primary teaching signal, and other terms ensure semantic alignment and spatial regularity.

In summary, ABounD (i) unifies concept adaptation and

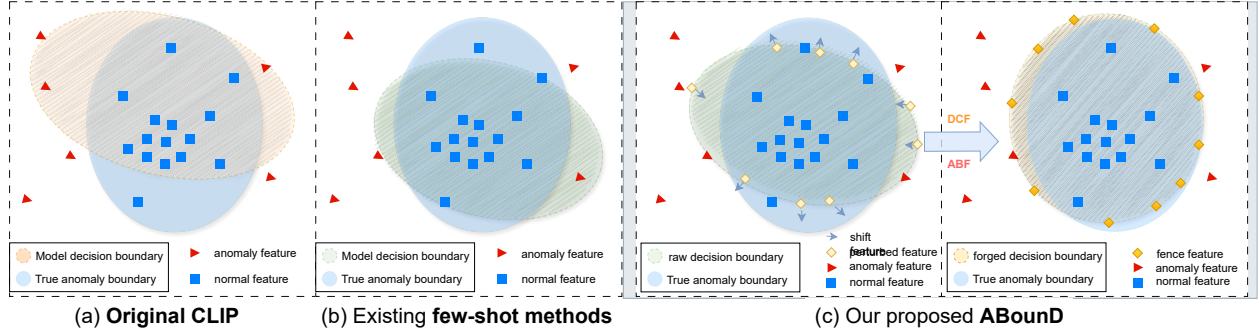


Figure 1. Decision boundary intuition for few-shot multi-class anomaly detection. (a) *Original CLIP* [16] forms a loose boundary that overlaps anomalies, causing false negatives. (b) *Existing few-shot methods* [9, 25, 26] often yield overly tight or vague boundaries: atypical but normal samples are rejected, while subtle defects are overlooked. (c) **ABounD** jointly learns **Dynamic Concept Fusion (DCF)** and **Adversarial Boundary Forging (ABF)**. DCF produces class-adaptive prompts; ABF forges fence features via PGD [14] to shape a sharp, normal-hugging decision boundary. The whole framework is optimized in a unified single stage under the *Concept-Boundary Loss (CBL)*.

adversarial boundary forging, (ii) forges boundary-level hard examples that align with the evolving feature manifold, and (iii) achieves state-of-the-art in the task of few-shot multi-class anomaly detection on MVTec-AD and VisA datasets.

2. Related Work

2.1. Industrial Anomaly Detection

Traditional methods for industrial anomaly detection can be broadly classified into two categories: reconstruction-based and feature embedding-based. Reconstruction methods, such as autoencoders [1] and diffusion models [20], identify anomalies through large reconstruction errors. Feature embedding methods, leveraging pre-trained backbones like ImageNet [4], model normal feature spaces and flag test samples whose features fall outside these spaces. Notable approaches include PatchCore [17], which uses a memory bank of patch-level features, and flow-based methods [5], which map normal features onto a simple distribution. While these methods have demonstrated strong performance, they typically follow a “one-model-per-class” paradigm—necessitating separate models and a large number of normal samples for each new object category. This design limits scalability and adaptability in dynamic industrial settings. In contrast, our approach overcomes this constraint by harnessing the generalization capabilities of large pre-trained vision-language models.

2.2. VLMs for Zero-/Few-shot Anomaly Detection

The advent of vision-language models (VLM) such as CLIP [16] has introduced a new paradigm for anomaly detection. By aligning visual and textual representations, these models can perform zero-shot or few-shot detection using natural language prompts. Early efforts like WinCLIP [7] demonstrated this potential by using manually crafted prompts to

score image patches. To move beyond the limitations of manual engineering, subsequent research has focused on prompt learning. Methods like PromptAD [9] learn continuous vector representations for “normal” and “abnormal” concepts. However, these learned prompts are often static and do not capture the category-specific semantics of different defects. Other strategies have pursued generic, object-agnostic prompts, either by using auxiliary datasets [3, 25] or residual learning [26], but these can require extensive annotated data or struggle with localization. Concurrently, other state-of-the-art approaches [12] have incorporated heavyweight modules to better bridge the modality gap, but at the cost of significant computational overhead and increased model complexity. More critically, these prompt-learning methods primarily focus on optimizing the *semantic concepts* but often fail to explicitly sculpt the *decision boundary* itself. In the few-shot regime, this ambiguity can lead to loose margins that misclassify atypical normal samples or overlook subtle defects. Our framework, ABounD, is designed precisely to address this gap by adversarially shaping the decision boundary.

3. Methodology

Our ABounD is a unified learning framework designed to be explicitly Boundary-Driven, built upon two synergistic components operating in concert. The **Dynamic Concept Fusion (DCF)** serves as the *anchor*, generating the sharp, class-adaptive concepts that define the “normal” vs. “abnormal” territories, while the **Adversarial Boundary Forging (ABF)** acts as the *driver*, leveraging these concepts to actively sculpt the decision frontier. This unified framework is trained in a single stage, optimizing both the prompt generator and the visual encoder jointly to achieve cohesive cross-modal alignment. The overall architecture of our framework is illustrated in Figure 2.

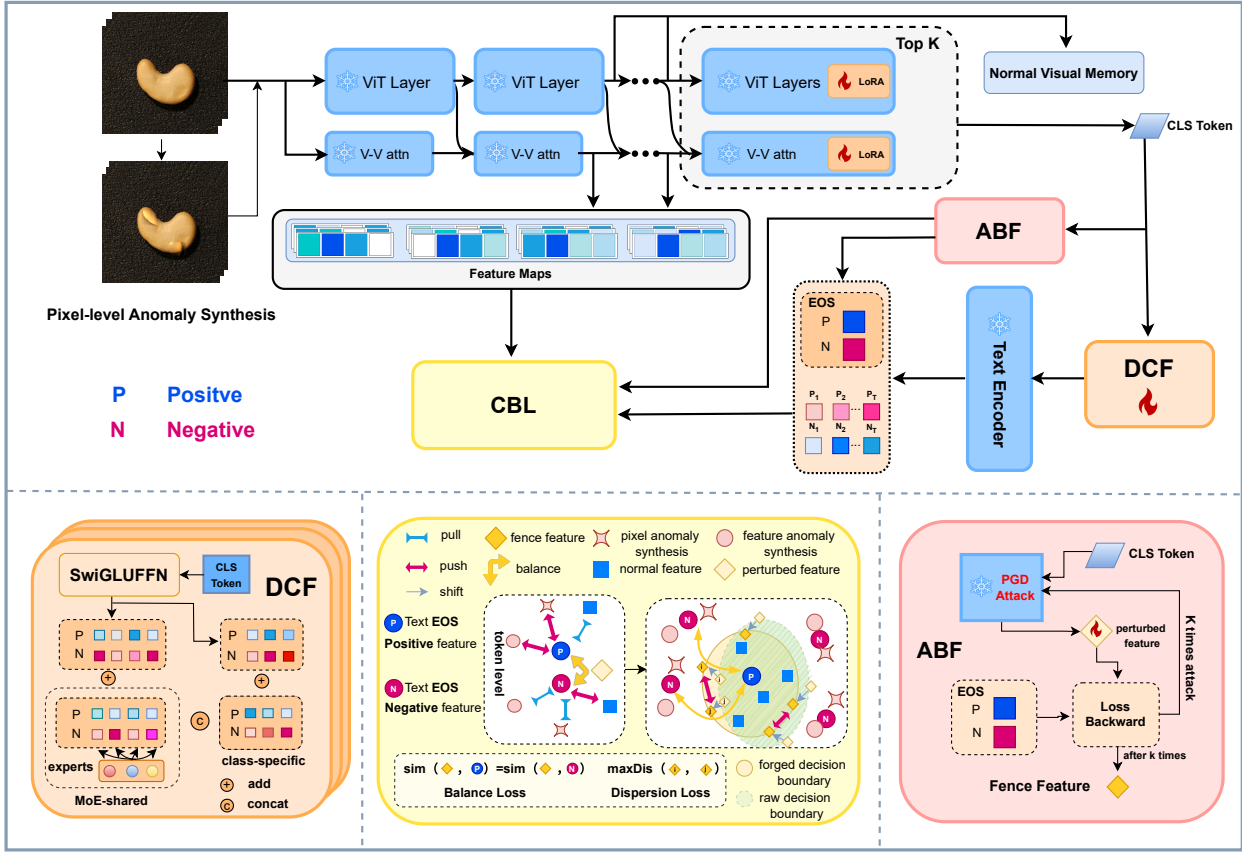


Figure 2. Overview of the **AbounD** framework, which introduces two core components: **Dynamic Concept Fusion (DCF)** and **Adversarial Boundary Forging (ABF)**. DCF dynamically generates class-adaptive prompts by fusing generalizable Mixture-of-Experts (MoE) semantics with learnable class-specific cues, conditioned on the global visual representation. ABF guides feature learning by performing PGD-based adversarial perturbations near the decision boundary, with balance and dispersion objectives ensuring well-distributed hard examples. The entire framework is optimized in a unified single-stage manner under the *Concept-Boundary Loss* (*CBL*), enabling robust few-shot multi-class anomaly detection.

3.1. Dynamic Concept Fusion

To enable instance-aware and class-adaptive anomaly detection, we propose a Dynamic Concept Fusion (DCF) module to generate both “shallow” prompts, which are prepended to the input layer embeddings, and “deep” prompts, which are injected into the intermediate layers of the text encoder. For the DCF module of depth n , we generate one shallow prompt and $n-1$ deep prompts. Each prompt, whether shallow or deep, is composed of two semantic axes: a shared component encoding general anomaly concepts (e.g., “flawless,” “damaged”) and a class-specific component capturing category-unique attributes (e.g., “bottle thread,” “transistor leg”). This entire mechanism is dynamically conditioned on the input image’s global visual features, allowing the model to construct discriminative prompts tailored to both normal and abnormal states in parallel.

Mixture-of-Experts for Shared Prompt. To enable the shared prompt to adapt to individual input, we use a

Mixture-of-Experts (MoE) framework. Instead of a single static prompt, we maintain a dictionary of K learnable expert prompts $\{\mathbf{E}_1, \dots, \mathbf{E}_K\}$. The gating network takes the global visual feature vector \mathbf{v}_{cls} of the input image and generates expert weights:

$$\mathbf{w} = \text{Softmax}(\text{MLP}_{\text{gate}}(\mathbf{v}_{\text{cls}})). \quad (1)$$

The MoE-shared prompt \mathbf{P}_{sa} is then synthesized as a weighted sum of these experts:

$$\mathbf{P}_{\text{sa}} = \sum_{k=1}^K w_k \cdot \mathbf{E}_k. \quad (2)$$

where w_k is the weight assigned to expert k . This MoE framework allows dynamic prompt construction while maintaining parameter efficiency, reducing overfitting and integrating general knowledge, making it suitable for few-shot settings.

Instance-Specific Modulation. To enhance the adaptive capability of the MoE-shared prompt \mathbf{P}_{sa} and class-specific prompt \mathbf{P}_{sp} , we introduce instance-specific modulation using a SwiGLU [18] Feed-Forward Network (FFN). This network generates small parameter offsets for both shared and class-specific parts of the shallow prompt, ensuring low parameter overhead while maintaining computational efficiency.

$$\delta_{\text{sa}} = \text{SwiGLUFFN}_{\text{sa}}(\mathbf{v}_{\text{cls}}) \quad (3)$$

$$\delta_{\text{sp}} = \text{SwiGLUFFN}_{\text{sp}}(\mathbf{v}_{\text{cls}}) \quad (4)$$

Hierarchical Prompt Assembly. The final assembly process differs slightly for shallow and deep prompts, reflecting their distinct roles. The shallow prompt incorporates all components: the MoE-generated base, the static class-specific base, and the instance-specific modulations. The final shallow prompt $\mathbf{P}_{\text{shallow}}$ is constructed as follows:

$$\mathbf{P}_{\text{shallow}} = \text{Concat}[(\mathbf{P}_{\text{sa}} + \delta_{\text{sa}}), (\mathbf{P}_{\text{sp}} + \delta_{\text{sp}})] \quad (5)$$

For deep prompts, which are injected into intermediate layers, instance-specific modulation is omitted to maintain stability and avoid overfitting across the model’s depth. The deep prompt at each layer $i \in [1, n - 1]$ is formed by concatenating the dynamically generated shared part and the learned class-specific part:

$$\mathbf{P}_{\text{deep}}^{(i)} = \text{Concat} \left[\mathbf{P}_{\text{sa}}^{(i)}, \mathbf{P}_{\text{sp}}^{(i)} \right] \quad (6)$$

This approach reduces overfitting by limiting parameters in deeper layers, while ensuring each layer’s guidance is contextually relevant and aligned with LoRA-fine-tuned visual features. This hierarchical prompt strategy ensures fine-grained adaptive conditioning signals without sacrificing efficiency.

3.2. Adversarial Boundary Forging

To learn a robust and discriminative decision boundary, we introduce the Adversarial Boundary Forging (ABF) module, pioneering the “fence” idea [15] for multi-modal CLIP anomaly detection. Our approach operates in two sequential phases within each training step: (1) generating adversarial features that reside on the boundary, and (2) leveraging these features to train the model.

Phase 1: Adversarial Feature Generation. To explicitly model the decision frontier, ABF generates adversarial features that lie close to the separating boundary between normal and abnormal distributions. Starting from a batch of global image features $\mathbf{v}_{\text{cls}}^1, \mathbf{v}_{\text{cls}}^2, \dots, \mathbf{v}_{\text{cls}}^N$, where each \mathbf{v}_{cls} denotes the [CLS] token representation from a normal sample,

we apply a Projected Gradient Descent (PGD) [14] procedure to iteratively perturb the features, yielding adversarial counterparts $\mathbf{v}_{\text{adv}}^1, \mathbf{v}_{\text{adv}}^2, \dots, \mathbf{v}_{\text{adv}}^N$.

Unlike precomputing similarity matrices [5, 17, 23], which assume a fixed and globally smooth metric space, our iterative perturbation dynamically adapts to the evolving embedding manifold, ensuring that the forged features remain on the *local* decision frontier even as the feature space shifts during training.

$$\mathcal{L}_{\text{attack}} = \mathcal{L}_{\text{balance}} + \beta \mathcal{L}_{\text{dispersion}}, \quad (7)$$

where β balances the trade-off between boundary alignment and sample diversity.

Balance Loss. Encourages each adversarial feature $\mathbf{v}_{\text{adv}}^i$ to be equally similar to both normal and abnormal text embeddings $(\mathbf{p}_{\text{pos}}, \mathbf{p}_{\text{neg}})$, positioning it near the true decision boundary:

$$\mathcal{L}_{\text{balance}} = |\text{sim}(\mathbf{v}_{\text{adv}}^i, \mathbf{p}_{\text{pos}}) - \text{sim}(\mathbf{v}_{\text{adv}}^i, \mathbf{p}_{\text{neg}})|. \quad (8)$$

Here, $\text{sim}(\cdot, \cdot)$ is the cosine similarity computed after L_2 normalizing both the visual and text features.

Dispersion Loss. Promotes diversity among generated boundary samples by maximizing their average pairwise distance:

$$\mathcal{L}_{\text{dispersion}} = -\frac{1}{N(N-1)/2} \sum_{i < j} \|\mathbf{v}_{\text{adv}}^i - \mathbf{v}_{\text{adv}}^j\|_2. \quad (9)$$

Phase 2: Boundary-Aware Model Training. Crucially, once the PGD attack concludes and returns the batch of “fence” features $\{\mathbf{v}_{\text{adv}}^i\}$, they are explicitly detached from the computation graph.

These static, gradient-less features are then immediately used to compute our boundary-shaping loss, \mathcal{L}_{ABF} , which is a main component of the overall *Concept-Boundary Loss (CBL)*. The goal of \mathcal{L}_{ABF} is to train the model to be maximally uncertain about these boundary samples by maximizing their predictive entropy (implemented as minimizing negative entropy):

$$\mathcal{L}_{\text{ABF}} = - \sum_{c \in \{\text{pos}, \text{neg}\}} P(c|\mathbf{v}_{\text{adv}}^i) \log P(c|\mathbf{v}_{\text{adv}}^i). \quad (10)$$

The probabilities $P(c|\mathbf{v}_{\text{adv}}^i)$ are computed by applying a softmax function with a temperature of 0.1 to the cosine similarity logits.

This process ensures that gradients from \mathcal{L}_{ABF} **do not** propagate back through the PGD generation. Instead, $\mathcal{L}_{\text{attack}}$ acts as a probe to find the boundary, and \mathcal{L}_{ABF} acts as the regularizer that trains the model to sculpt it. This provides the guiding supervision that integrates with the other semantic and spatial terms of CBL.

3.3. Training and Inference

Unified training. **ABounD** adopts a unified single-stage optimization where both the **Dynamic Concept Fusion (DCF)** module and the LoRA-tuned visual encoder are updated jointly, while the rest of CLIP remains frozen. Training is governed by the *Concept-Boundary Loss (CBL)*, under the guidance of **Adversarial Boundary Forging (ABF)**, which shapes the decision margin and regulates the remaining terms:

$$\mathcal{L}_{\text{CBL}} = \lambda_{\text{abf}} \mathcal{L}_{\text{ABF}} + \lambda_{\text{psg}} \mathcal{L}_{\text{PSG}} + \lambda_{\text{seg}} \mathcal{L}_{\text{SEG}}, \quad (11)$$

ABF-guided regularization: **Prompt Semantic Grounding Loss** (\mathcal{L}_{PSG}) operates on *normal* images to ensure the DCF-generated prompts are semantically meaningful. It aligns the prompts with both text anchors and corresponding visual patch features at coarse and fine-grained levels. [12] **Pixel-level segmentation loss** (\mathcal{L}_{SEG}) provides spatial supervision using synthetic anomalies generated via a cut-and-paste strategy [10]. Detailed formulations of \mathcal{L}_{PSG} and \mathcal{L}_{SEG} are provided in the Supplementary Material.

Intuitively, \mathcal{L}_{ABF} provides boundary-driven supervision by generating and exploiting adversarial fence features, while \mathcal{L}_{PSG} provides semantic regularization (on normal data) and \mathcal{L}_{SEG} provides spatial regularization (on synthetic data). This design prioritizes boundary shaping while keeping auxiliary terms concise, resulting in a sharp and robust decision margin for few-shot multi-class anomaly detection.

Inference. During inference, our model operates in a class-agnostic, one-for-all manner, adapting the scoring process from prior work.

Class-Agnostic Identification. For each class k seen during training, we model its normal samples with a multivariate normal distribution defined by the mean μ_k and the covariance Σ_k of their global visual features. For a test image, we identify its most probable class k_m by finding the distribution with the highest log-likelihood.

Memory-Fused Anomaly Score. Once the predicted class k_m is determined, we retrieve its corresponding multi-level visual and textual memory banks. The final anomaly score is a fusion of the text-driven and visual-driven scores. The text score compares patch features with instance-specific prompts fused with embeddings from the text memory bank. The visual score measures the dissimilarity of each test patch to its nearest neighbor in the visual memory bank. The final anomaly map is a weighted sum of these scores, and the image-level score is the maximum value from this map.

$$\mathbf{M} = \mathbf{M}_{\text{text}} + \mathbf{M}_{\text{vis}}, \quad S = \max(\mathbf{M}), \quad (12)$$

where \mathbf{M}_{text} is the patch-text similarity map, and \mathbf{M}_{vis} is the visual distance map from multi-layer normal feature memories.

4. Experiments

4.1. Experimental Setup

Datasets. We conduct experiments on two widely-used benchmarks: MVTec-AD [1] and VisA [27]. MVTec-AD comprises 15 texture and object categories, while VisA includes 12 categories with more diverse and complex structures. Following the standard one-class anomaly detection protocol, only normal images are used for training. The test sets contain both normal and anomalous samples, accompanied by pixel-level annotations for localization tasks.

Evaluation Metrics. Following prior work, we evaluate image-level performance using AUROC (Area Under the Receiver Operating Characteristic Curve) and AUPR (Area Under the Precision–Recall Curve), and pixel-level performance using AUROC and PRO (Per-Region Overlap), providing a comprehensive assessment of both detection and localization.

Additional Implementation Details.. Our framework follows a unified implementation across all datasets and experiments. All models are trained for 20 epochs using 224×224 inputs with a ViT-L/14 visual backbone kept frozen except for a small set of top layers adapted via LoRA (rank $r=4$). Both the Dynamic Concept Fusion (DCF) module and the LoRA adapter are optimized jointly throughout training, whereas all remaining model parameters remain frozen.

The DCF module is implemented as a 7-layer deep prompt generator, where each layer contains a lightweight mixture-of-experts (MoE) unit with four experts. The module receives a normalized global feature as input and outputs a pair of positive and negative context prompts, together with a set of deep prompt embeddings. This design is fixed for all experiments; dataset differences only affect the choice of prompt length but not the architecture.

The Adversarial Boundary Forging (ABF) module is implemented as a projected gradient descent (PGD) procedure operating directly in the normalized global feature space. The attack runs for 10 steps with step size $\alpha = 1$ and an L_∞ perturbation radius of $\epsilon = 10$. At each step, the adversarial feature is optimized using a balance loss that enforces equidistance to the positive and negative textual concepts and a dispersion regularizer that encourages diversity among boundary samples. The resulting “fence” features are used only during training and do not modify inference-time behavior.

All experiments employ a unified data pipeline: images are resized to 224×224 , and for each class the first k training images are used for the k -shot setting without manual selection. Memory banks for global features, patch features (four transformer layers), and textual prompts are built with the same procedure for every dataset. Following training, the class-specific memory banks store normalized global

Setup	Method	MVTec-AD				VisA			
		Image-level		Pixel-level		Image-level		Pixel-level	
		AUROC	AUPR	AUROC	PRO	AUROC	AUPR	AUROC	PRO
0-shot	WinCLIP	89.1	95.0	81.1	62.3	73.3	76.3	79.8	57.9
	AnomalyCLIP	91.5	96.2	91.1	81.4	82.1	85.4	95.5	87.0
1-shot	PatchCore	63.7	81.2	83.9	72.7	58.9	62.8	76.7	64.3
	WinCLIP	92.8	96.5	92.4	83.5	83.1	85.1	94.6	80.9
	PromptAD*	90.9 \pm 0.4	95.0 \pm 0.3	93.6 \pm 0.2	87.3 \pm 0.2	85.9 \pm 0.7	87.8 \pm 0.5	96.1 \pm 0.3	82.2 \pm 0.9
	InCTRL	-	-	-	-	-	-	-	-
	IIPAD*	93.8 \pm 0.3	97.0 \pm 0.2	95.7 \pm 0.2	89.7 \pm 0.2	84.9 \pm 0.6	87.2 \pm 0.4	96.5 \pm 0.2	86.7 \pm 0.6
	ABounD	94.8\pm0.1	97.5\pm0.1	96.2\pm0.1	91.1\pm0.1	87.3\pm0.3	89.0\pm0.3	97.4\pm0.1	88.6\pm0.2
2-shot	PatchCore	72.4	86.2	89.6	74.2	60.2	64.3	82.4	68.1
	WinCLIP	92.7	96.3	92.4	83.9	83.7	84.9	95.1	81.8
	PromptAD*	91.5 \pm 0.3	95.5 \pm 0.3	93.9 \pm 0.2	88.0 \pm 0.2	86.7 \pm 0.7	89.5 \pm 0.7	96.7 \pm 0.3	81.6 \pm 0.6
	InCTRL	94.0 \pm 1.5	96.9 \pm 0.4	-	-	85.8 \pm 2.2	87.7 \pm 1.6	-	-
	IIPAD*	95.6 \pm 0.3	97.8 \pm 0.2	96.2 \pm 0.3	90.3 \pm 0.2	85.9 \pm 0.5	88.0 \pm 0.5	96.8 \pm 0.2	87.5 \pm 0.5
	ABounD	96.8\pm0.1	98.2\pm0.1	96.6\pm0.1	91.9\pm0.1	89.4\pm0.3	91.8\pm0.3	97.5\pm0.1	88.9\pm0.2
4-shot	PatchCore	74.9	88.8	92.6	80.8	62.6	69.9	85.4	70.6
	WinCLIP	94.0	96.9	92.9	84.4	84.1	86.1	95.2	82.1
	PromptAD*	93.4 \pm 0.3	96.5 \pm 0.3	94.3 \pm 0.1	88.4 \pm 0.2	86.9 \pm 0.9	89.7 \pm 1.1	96.7 \pm 0.3	82.0 \pm 0.8
	InCTRL	94.5 \pm 1.8	97.2 \pm 0.6	-	-	87.7 \pm 1.9	90.2 \pm 2.7	-	-
	IIPAD*	96.1 \pm 0.2	97.9 \pm 0.1	96.4 \pm 0.1	90.8 \pm 0.2	87.8 \pm 0.9	88.9 \pm 0.8	97.0 \pm 0.1	87.8 \pm 0.5
	ABounD	97.0\pm0.1	98.3\pm0.1	96.9\pm0.1	92.3\pm0.1	90.3\pm0.8	92.4\pm0.6	97.6\pm0.2	89.2\pm0.3

Table 1. Overview of anomaly detection and localization performance under the one-for-all paradigm on MVTec-AD and VisA datasets. The best-performing results are indicated in **bold**, while the second-best are underlined. Methods marked with * indicate results obtained from our local reproduction over 10 independent runs, reported as mean \pm standard deviation. The results for InCTRL are incomplete as it only reports image-level accuracy and utilizes an additional dataset, which was not reproduced in this work.

means and covariances, token-level patch features, and averaged positive/negative textual embeddings, enabling unified anomaly scoring during inference.

This supplementary section summarizes the implementation components that remain consistent across all datasets and evaluations and reflects the default system behavior encoded in our released source code.

Baselines. To validate the effectiveness of our proposed method, we conduct comprehensive comparisons against several state-of-the-art training-free and CLIP-based anomaly detection methods, including PatchCore [17], WinCLIP [7], PromptAD [9], InCTRL [26], AnomalyCLIP [25] and IIPAD [12]. Furthermore, we extend our evaluation to recent full-shot one-for-all anomaly detection approaches, such as UniAD [22], OmniAL [24], HVQ-Trans [11], and DiAD [6]. All baseline results under the one-for-all paradigm are taken from the IIPAD [12] paper, except for methods marked with *, which were reproduced locally over 10 independent runs. Our proposed ABounD is independently implemented and evaluated under the same experimental settings to ensure fair and consistent compar-

ison.

ViT Backbone	MVTec-AD		VisA	
	AUROC _I	AUROC _P	AUROC _I	AUROC _P
ViT-B/16	91.3	95.5	83.9	96.8
ViT-L/14	94.8	96.2	87.3	97.4
ViT-L/14@336px	96.2	96.3	89.3	97.8

Table 2. Ablation study of ViT backbone architectures under the 1-shot one-for-all setting (ViT-L/14@336px uses 336 \times 336 inputs).

4.2. Experimental Results

Table 1 presents the experimental results on the MVTec-AD and VisA datasets under different few-shot settings, where all methods follow the one-for-all paradigm. Our proposed **ABounD** achieves **state-of-the-art performance across all metrics and shot settings**. As shown in Table 2, our method is effective across different ViT backbones. This further demonstrates the robustness of ABounD, which generalizes well regardless of the underlying backbone architecture.

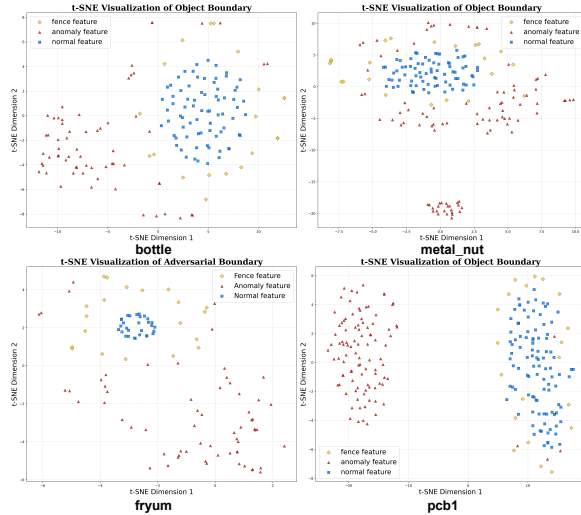


Figure 3. t-SNE visualization of the learned feature space for representative classes under the 1-shot setting: “bottle” and “metal_nut” from MVTec-AD, and “fryum” and “pcb1” from VisA.

Method	Setup	MVTec-AD		VisA	
		AUROC _I	AUROC _P	AUROC _I	AUROC _P
Ours	2-shot	96.8	96.6	89.4	97.5
	4-shot	97.0	96.9	90.3	97.6
	32-shot	97.7	97.5	93.3	98.6
UniAD	Full-shot	96.5	96.8	91.9	98.6
OmniAL	Full-shot	97.2	98.3	87.8	96.6
DiAD	Full-shot	97.2	96.8	86.8	96.0
HVQ-Trans	Full-shot	98.0	97.3	93.2	98.7

Table 3. Comparison with full-shot methods on MVTec-AD and VisA. Our few-shot results are competitive, though the training data scale differs.

Method	Params	Training VRAM	Inference VRAM
IIPAD	427+560M	23.98G	9.98G
Ours	427+41M	3.6G	2.5G

Table 4. Resource consumption comparison with other methods on MVTec-AD under the 1-shot setting. “427M” refers to the ViT-L/14 model.

Metric	WinCLIP	PromptAD	IIPAD	Ours
Im/s	9.42	12.39	8.18	11.66

Table 5. Throughput(Im/s, image per second) comparison with other methods on MVTec-AD under the 1-shot setting.

It is noteworthy that **IIPAD** [12] uses an additional pre-trained **Q-former** module from BLIP [8] to improve

visual-textual alignment. While this boosts performance, it also increases model complexity and resource demand. In contrast, ABounD achieves superior results with a lightweight, CLIP-based architecture, without relying on extra pre-trained modules.

Moreover, as shown in Table 3, ABounD matches or surpasses several full-shot methods, even outperforming some with just 32 normal samples. In terms of efficiency, Table 4 demonstrates that ABounD requires substantially fewer parameters and GPU memory during both training and inference. This efficiency is further reflected in Table 5, where our method achieves competitive inference throughput (Im/s), demonstrating that it is not only accurate but also practical for deployment. These results validate the effectiveness of our approach in achieving robust anomaly detection under few-shot settings.

Qualitative Visualization. To better understand how **ABounD** organizes its learned feature manifold, we visualize the **1-shot visual embeddings** using t-SNE, as shown in Fig. 3. Specifically, each point represents a visual feature vector extracted from the CLIP visual encoder ViT-L/14 after **LoRA/DCF** adaptation. The synthetic boundary samples generated by **ABF** are included in the same embedding space.

For illustration, we sample representative categories from both benchmarks: “bottle” and “metal_nut” from MVTec-AD, and “fryum” and “pcb1” from VisA. The resulting t-SNE plots reveal that normal and abnormal features form compact and clearly separated clusters, indicating strong cross-modal alignment. The additional boundary features forged by the Adversarial Boundary Forging (ABF) module are distributed between these clusters, demonstrating that ABF effectively regularizes the embedding space and sharpens the decision boundary.

The qualitative results of anomaly localization are further shown in Figure 4. Compared to PromptAD and IIPAD, our method generates more precise and cleaner localization maps for both MVTec-AD and VisA. ABounD maintains consistent performance across object and texture categories in the 1-shot setting and can accurately delineate small or subtle defect regions.

4.3. Ablation Studies

We conduct ablation studies to evaluate the individual contributions of our framework’s key components. All experiments are performed on the MVTec-AD and VisA datasets under the 1-shot setting to rigorously test their effectiveness under data scarcity.

Effectiveness of Dynamic Concept Fusion. The Dynamic Concept Fusion (DCF) module generates adaptive prompts that capture both class-level and instance-specific information. As shown in Table 6, using a static prompt

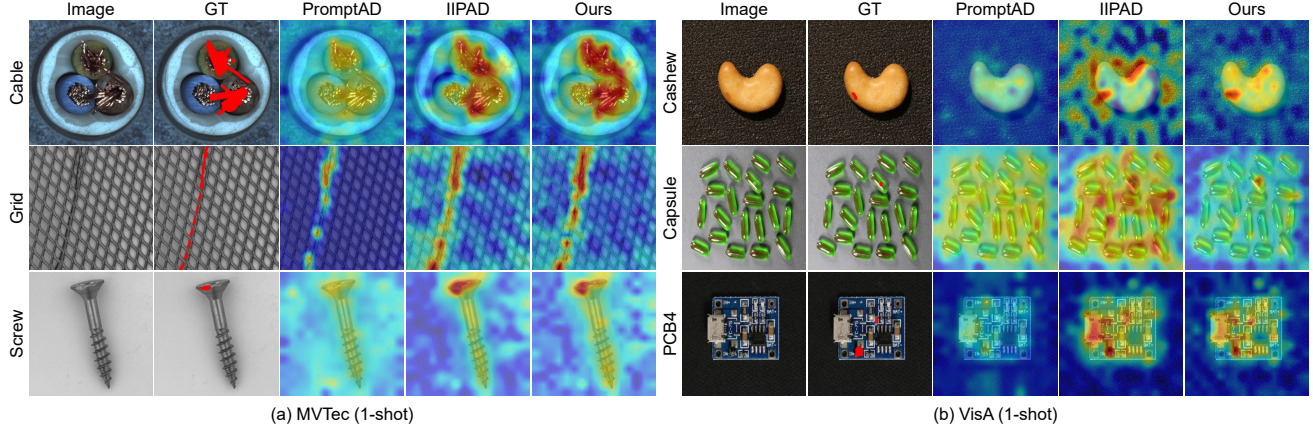


Figure 4. Qualitative visualization of anomaly localization results on MVTec-AD and VisA under the 1-shot setting. Compared methods include PromptAD, IIPAD, and our ABounD. Our method achieves clearer and more precise localization boundaries, particularly on small or fine-grained anomaly regions.

MoE	Specific	MVTec-AD		VisA	
		AUROC _I	AUROC _P	AUROC _I	AUROC _P
×	×	93.4	94.3	84.9	95.2
×	✓	94.1	95.4	86.4	95.8
✓	×	94.6	95.7	86.9	97.2
✓	✓	94.8	96.2	87.3	97.4

Table 6. Ablation study of the Dynamic Concept Fusion (DCF) module under the 1-shot setting. The baseline (×, ×) uses a simple, static learnable prompt. “MoE” refers to the instance-aware Mixture-of-Experts component, and “Specific” refers to the class-specific prompt vectors.

yields the lowest performance. Introducing class-specific prompts improves detection and localization, and incorporating the instance-aware MoE mechanism further boosts performance. The best results are obtained when both components are combined, highlighting the importance of hierarchical prompt adaptation.

$\mathcal{L}_{\text{balance}}$	$\mathcal{L}_{\text{dispersion}}$	MVTec-AD		VisA	
		AUROC _I	AUROC _P	AUROC _I	AUROC _P
×	×	92.7	95.3	84.9	96.2
×	✓	92.5	94.7	84.7	96.0
✓	×	94.4	95.7	87.0	96.8
✓	✓	94.8	96.2	87.3	97.4

Table 7. Ablation study of the Adversarial Boundary Forging (ABF) loss components under the 1-shot setting. “✓” indicates the loss is included; “×” indicates it is excluded.

Effectiveness of Adversarial Boundary Forging. The Ad-

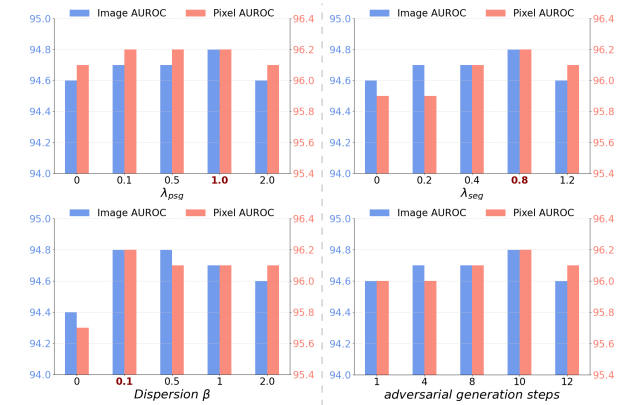


Figure 5. Image/pixel AUROC on MVTec-AD under 1-shot setting using different settings of λ_{psg} , λ_{seg} , $\text{dispersion } \beta$, and $\text{adversarial generation steps}$.

versarial Boundary Forging (ABF) module actively shapes a sharp decision boundary by leveraging hard examples. Table 7 demonstrates that removing ABF causes a performance drop. Using only the dispersion loss degrades performance, indicating that promoting feature diversity without directional guidance can be counterproductive. In contrast, the balance loss alone significantly improves results, confirming its primary role in boundary formation. The combination of both losses yields the best performance, where the balance loss positions the boundary and the dispersion loss regularizes it with diverse exemplars, resulting in a robust defense against anomalies.

4.4. Hyper-parameter Analysis

As Figure 5 illustrates, our framework is exceptionally robust to its hyper-parameter settings. We analyze this from

two perspectives: First, for the supplementary loss weights, λ_{PSG} and λ_{SEG} (top row), performance remains high and stable across a broad range of values. This strongly supports our “Boundary-Driven” thesis: the training is principally guided by **ABF**, reducing these other losses to the role of simple stabilizers. Second, for **ABF**’s own internal parameters (bottom row), it is also not overly sensitive, showing wide, stable optimal ranges for both the *dispersion* β and the *adversarial generation steps*. This stability ensures the framework maintains a robust decision boundary, making it highly effective in practical applications.

5. Conclusion

In this paper, we proposed **ABounD**, a unified, Adversarial Boundary-Driven learning framework for few-shot multi-class anomaly detection. Our method combines two components to establish a highly discriminative decision margin: Dynamic Concept Fusion (DCF) defines the “conceptual anchors” for the boundary, while Adversarial Boundary Forging (ABF) actively *fortifies* the boundary itself. Optimized jointly under a *Concept-Boundary Loss*, this synergy yields a feature space that is both robustly aligned and highly discriminative. Extensive experiments on MVTec-AD and VisA validate that **ABounD** achieves state-of-the-art performance in the challenging few-shot, multi-class setting. Future work will focus on broader applications and improved training efficiency.

References

- [1] Paul Bergmann, Michael Fauser, David Sattlegger, and Carsten Steger. Mvtac ad—a comprehensive real-world dataset for unsupervised anomaly detection. In *Proceedings of the IEEE/CVF conference on computer vision and pattern recognition*, pages 9592–9600, 2019. [2](#) [5](#)
- [2] Ioana Bica, Anastasija Ilić, Matthias Bauer, Goker Erdogan, Matko Bošnjak, Christos Kaplanis, Alexey A Gritsenko, Matthias Minderer, Charles Blundell, Razvan Pascanu, et al. Improving fine-grained understanding in image-text pre-training. *arXiv preprint arXiv:2401.09865*, 2024. [3](#)
- [3] Yunkang Cao, Jiangning Zhang, Luca Frittoli, Yuqi Cheng, Weiming Shen, and Giacomo Boracchi. Adaclip: Adapting clip with hybrid learnable prompts for zero-shot anomaly detection. In *European Conference on Computer Vision*, pages 55–72. Springer, 2024. [2](#)
- [4] Jia Deng, Wei Dong, Richard Socher, Li-Jia Li, Kai Li, and Li Fei-Fei. Imagenet: A large-scale hierarchical image database. In *2009 IEEE conference on computer vision and pattern recognition*, pages 248–255. Ieee, 2009. [2](#)
- [5] Denis Gudovskiy, Shun Ishizaka, and Kazuki Kozuka. Cflow-ad: Real-time unsupervised anomaly detection with localization via conditional normalizing flows. In *Proceedings of the IEEE/CVF winter conference on applications of computer vision*, pages 98–107, 2022. [2](#) [4](#)
- [6] Haoyang He, Jiangning Zhang, Hongxu Chen, Xuhai Chen, Zhishan Li, Xu Chen, Yabiao Wang, Chengjie Wang, and Lei Xie. A diffusion-based framework for multi-class anomaly detection. In *Proceedings of the AAAI conference on artificial intelligence*, pages 8472–8480, 2024. [6](#)
- [7] Jongheon Jeong, Yang Zou, Taewan Kim, Dongqing Zhang, Avinash Ravichandran, and Onkar Dabeer. Winclip: Zero-/few-shot anomaly classification and segmentation. In *Proceedings of the IEEE/CVF Conference on Computer Vision and Pattern Recognition*, pages 19606–19616, 2023. [1](#) [2](#) [6](#)
- [8] Junnan Li, Dongxu Li, Silvio Savarese, and Steven Hoi. Blip-2: Bootstrapping language-image pre-training with frozen image encoders and large language models. In *International conference on machine learning*, pages 19730–19742. PMLR, 2023. [7](#)
- [9] Xiaofan Li, Zhizhong Zhang, Xin Tan, Chengwei Chen, Yanyun Qu, Yuan Xie, and Lizhuang Ma. Promptad: Learning prompts with only normal samples for few-shot anomaly detection. In *Proceedings of the IEEE/CVF Conference on Computer Vision and Pattern Recognition*, pages 16838–16848, 2024. [1](#) [2](#) [6](#)
- [10] Zhikang Liu, Yiming Zhou, Yuansheng Xu, and Zilei Wang. Simplenet: A simple network for image anomaly detection and localization. In *Proceedings of the IEEE/CVF conference on computer vision and pattern recognition*, pages 20402–20411, 2023. [5](#) [3](#)
- [11] Ruiying Lu, YuJie Wu, Long Tian, Dongsheng Wang, Bo Chen, Xiyang Liu, and Ruimin Hu. Hierarchical vector quantized transformer for multi-class unsupervised anomaly detection. *Advances in Neural Information Processing Systems*, 36:8487–8500, 2023. [6](#)
- [12] Wenxi Lv, Qinliang Su, and Wencho Xu. One-for-all few-shot anomaly detection via instance-induced prompt learning. In *The Thirteenth International Conference on Learning Representations*, 2025. [1](#) [2](#) [5](#) [6](#) [7](#) [4](#)
- [13] Wenxin Ma, Xu Zhang, Qingsong Yao, Fenghe Tang, Chenxu Wu, Yingtai Li, Rui Yan, Zihang Jiang, and S Kevin Zhou. Aa-clip: Enhancing zero-shot anomaly detection via anomaly-aware clip. In *Proceedings of the Computer Vision and Pattern Recognition Conference*, pages 4744–4754, 2025. [1](#)
- [14] Aleksander Madry, Aleksandar Makelov, Ludwig Schmidt, Dimitris Tsipras, and Adrian Vladu. Towards deep learning models resistant to adversarial attacks. *arXiv preprint arXiv:1706.06083*, 2017. [1](#) [2](#) [4](#)
- [15] Phuc Cuong Ngo, Amadeus Aristo Winarto, Connie Khor Li Kou, Sojeong Park, Farhan Akram, and Hwee Kuan Lee. Fence gan: Towards better anomaly detection. In *2019 IEEE 31St International Conference on tools with artificial intelligence (ICTAI)*, pages 141–148. IEEE, 2019. [4](#)
- [16] Alec Radford, Jong Wook Kim, Chris Hallacy, Aditya Ramesh, Gabriel Goh, Sandhini Agarwal, Girish Sastry, Amanda Askell, Pamela Mishkin, Jack Clark, et al. Learning transferable visual models from natural language supervision. In *International conference on machine learning*, pages 8748–8763. PMLR, 2021. [1](#) [2](#)
- [17] Karsten Roth, Latha Pemula, Joaquin Zepeda, Bernhard Schölkopf, Thomas Brox, and Peter Gehler. Towards total recall in industrial anomaly detection. In *Proceedings of*

the IEEE/CVF conference on computer vision and pattern recognition, pages 14318–14328, 2022. 2, 4, 6

- [18] Noam Shazeer. Glu variants improve transformer. *arXiv preprint arXiv:2002.05202*, 2020. 4
- [19] Hanxin Wang, Tian Liu, and Shu Kong. Robust few-shot vision-language model adaptation. *arXiv preprint arXiv:2506.04713*, 2025. 1
- [20] Julian Wyatt, Adam Leach, Sebastian M Schmon, and Chris G Willcocks. Anoddpm: Anomaly detection with denoising diffusion probabilistic models using simplex noise. In *Proceedings of the IEEE/CVF conference on computer vision and pattern recognition*, pages 650–656, 2022. 2
- [21] Zhenyu Yan, Qingqing Fang, Wenxi Lv, and Qinliang Su. Anomalyd: Few-shot multi-class anomaly detection with stable diffusion model. *arXiv preprint arXiv:2408.01960*, 2024. 1
- [22] Zhiyuan You, Lei Cui, Yujun Shen, Kai Yang, Xin Lu, Yu Zheng, and Xinyi Le. A unified model for multi-class anomaly detection. *Advances in Neural Information Processing Systems*, 35:4571–4584, 2022. 6
- [23] Vitjan Zavrtanik, Matej Kristan, and Danijel Skočaj. Draem—a discriminatively trained reconstruction embedding for surface anomaly detection. In *Proceedings of the IEEE/CVF international conference on computer vision*, pages 8330–8339, 2021. 4
- [24] Ying Zhao. Omnia: A unified cnn framework for unsupervised anomaly localization. In *Proceedings of the IEEE/CVF Conference on Computer Vision and Pattern Recognition*, pages 3924–3933, 2023. 6
- [25] Qihang Zhou, Guansong Pang, Yu Tian, Shibo He, and Jiming Chen. Anomalyclip: Object-agnostic prompt learning for zero-shot anomaly detection. *arXiv preprint arXiv:2310.18961*, 2023. 1, 2, 6
- [26] Jiawen Zhu and Guansong Pang. Toward generalist anomaly detection via in-context residual learning with few-shot sample prompts. In *Proceedings of the IEEE/CVF conference on computer vision and pattern recognition*, pages 17826–17836, 2024. 1, 2, 6
- [27] Yang Zou, Jongheon Jeong, Latha Pemula, Dongqing Zhang, and Onkar Dabeer. Spot-the-difference self-supervised pre-training for anomaly detection and segmentation. In *European conference on computer vision*, pages 392–408. Springer, 2022. 5
- [28] Zuo Zuo, Yao Wu, Baoqiang Li, Jiahao Dong, You Zhou, Lei Zhou, Yanyun Qu, and Zongze Wu. Clip-fsac: Boosting clip for few-shot anomaly classification with synthetic anomalies. In *Proceedings of the Thirty-Third International Joint Conference on Artificial Intelligence, IJCAI-24, International Joint Conferences on Artificial Intelligence Organization*, pages 1834–1842, 2024. 1

ABounD: Adversarial Boundary-Driven Few-Shot Learning for Multi-Class Anomaly Detection

Supplementary Material

A. Full Implementation Details

Data pre-processing. Following CLIP-style pre-processing, we employ the image transformation pipeline implemented in `VVCLIP_lib` for both MVTec-AD and VisA. Each RGB image is first converted to the $[0, 1]$ range, then normalized channel-wise using the OpenAI CLIP statistics with mean $[0.48145466, 0.4578275, 0.40821073]$ and standard deviation $[0.26862954, 0.26130258, 0.27577711]$. We adopt bicubic resizing based on the Pillow implementation, followed by a center crop to the target resolution. Unless otherwise specified, the input resolution is set to 224×224 so that all images are aligned with the ViT-L/14 backbone used in our framework. The same pre-processing is applied consistently to both training and test images in all experiments.

Hyper-parameters. We use a unified set of default hyper-parameters for all experiments unless otherwise specified. All models are trained for 20 epochs with batch size 1 using 224×224 images.

The Dynamic Concept Fusion (DCF) module is implemented as a 7-layer prompt generator. Each layer contains a lightweight mixture-of-experts block with four experts, and the prompt embeddings are divided into shared tokens and class-specific tokens. This architecture remains identical for all datasets; only the total prompt length and the number of class-specific tokens vary, as reported in the main paper.

The Adversarial Boundary Forging (ABF) module operates in the normalized global feature space of the visual encoder. It performs a 10-step PGD procedure with step size $\alpha = 1$ and an L_∞ perturbation radius of $\epsilon = 10$. Each step applies a balance loss that enforces equal cosine similarity to the normal and abnormal text embeddings, together with a dispersion term that promotes diversity among adversarial boundary samples. The PGD procedure is initialized with random noise and is used only during training.

Prompt-related parameters are optimized with Adam using a learning rate of 1.5×10^{-2} and weight decay 1×10^{-5} under a cosine-annealing schedule.

LoRA is applied to the query–key–value and output projection layers of the top transformer blocks of the ViT-L/14 encoder, using rank $r = 4$, scaling factor $\alpha = 8$, and dropout 0.25. For MVTec-AD, we finetune the top 12 blocks, while for VisA, we finetune the top 8 blocks. All remaining backbone parameters remain frozen. The LoRA learning rate is 2×10^{-5} on MVTec-AD and 1.7×10^{-4} on

VisA.

The loss weights for the segmentation loss, the prompt semantic grounding loss, and the ABF loss follow the values reported in the main paper and remain fixed for all experiments within each dataset.

Manual anomaly prompts. We adopt a unified prompt construction scheme shared across all datasets, following the general formulation of recent prompt-based anomaly detection methods [7, 9, 12]. The design combines a small set of generic anomaly descriptors (e.g., “damaged {}”, “abnormal {}”, “imperfect {}”) with object-specific suffixes that reflect common defect patterns for each category. These suffixes are instantiated by inserting the class name into the prompt templates. All suffix lists are predefined and fixed; no dataset-specific prompt tuning or per-class manual adjustment is applied in our experiments.

For each class, we pair its normal descriptors (e.g., “normal {}”, “flawless {}”) with the corresponding abnormal descriptors to form text templates, which are then combined with a small number of visual instruction templates such as “an industrial image of a {} for anomaly detection.” The resulting sentences are encoded by the CLIP text encoder and averaged to produce class-conditional normal and abnormal text embeddings.

The complete set of generic and object-customized anomaly suffixes used in our experiments is provided in the supplementary material (Fig. 6). This prompt schema is fixed for both MVTec-AD and VisA and remains unchanged across all k -shot settings.

Text Prompt Assembly. The final assembly of the text input sequence is a critical implementation detail. In our `main.py` script, we define a dictionary of static, manually specified prefix texts, `prefix_texts`, containing a small set of generic descriptors for both “normal” (e.g., “normal”, “flawless”, “perfect”) and “abnormal” (e.g., “defect”, “damaged”, “abnormal”) states. At initialization, these string-based prefixes are tokenized and converted into word embeddings, which are cached in a `prefix_embeddings` dictionary.

During training, at each iteration, one prefix embedding is randomly sampled for both the positive and negative prompts. This static prefix embedding p_{prefix} is passed to the `encode_text_with_prefix` function together with the dynamically generated DCF prompt p_{def} . We explicitly retain p_{prefix} in the assembled prompt because it provides a stable semantic anchor. While p_{def} adapts to image

```

1. Generic anomaly suffixes
'damaged {}', 'broken {}', '{} with flaw', '{} with defect', '{} with damage'

2. Object-customized anomaly suffixes (MVTec)
'bottle' : ['{} with large breakage', '{} with small breakage', '{} with contamination'],
'toothbrush' : ['{} with bent wire', '{} with anomaly'],
'carpet' : ['{} with hole', '{} with color stain', '{} with metal contamination',
            '{} with thread residue', '{} with thread', '{} with cut'],
'hazelnut' : ['{} with crack', '{} with cut', '{} with hole', '{} with print'],
'leather' : ['{} with color stain', '{} with cut', '{} with fold', '{} with glue'],
'cable' : ['{} with bent wire', '{} with missing part', '{} with missing wire',
            '{} with cut', '{} with poke'],
'capsule' : ['{} with crack', '{} with faulty imprint', '{} with poke',
            '{} with scratch', '{} squeezed with compression'],
'grid' : ['{} with breakage', '{} with thread residue', '{} with thread',
            '{} with metal contamination', '{} with glue', '{} with a bent shape'],
'pill' : ['{} with color stain', '{} with contamination', '{} with crack',
            '{} with faulty imprint', '{} with scratch', '{} with abnormal type'],
'transistor' : ['{} with bent lead', '{} with cut lead', '{} with damage',
                '{} with misplaced transistor'],
'metal_nut' : ['{} with a bent shape', '{} with color stain',
                '{} with a flipped orientation', '{} with scratch'],
'screw' : ['{} with manipulated front', '{} with scratch neck', '{} with scratch head'],
'zipper' : ['{} with broken teeth', '{} with fabric border', '{} with defect fabric',
            '{} with broken fabric', '{} with split teeth', '{} with squeezed teeth'],
'tile' : ['{} with crack', '{} with glue strip', '{} with gray stroke',
            '{} with oil', '{} with rough surface'],
'wood' : ['{} with color stain', '{} with hole', '{} with scratch', '{} with liquid']

```

3. Object-customized anomaly suffixes (VisA)

```

'candle' : ['{} with melded wax', '{} with foreign particals', '{} with extra wax',
            '{} with chunk of wax missing', '{} with weird candle wick',
            '{} with damaged corner of packaging', '{} with different colour spot'],
'capsules' : ['{} with scratch', '{} with discolor', '{} with missshape',
            '{} with leak', '{} with bubble'],
'cashew' : ['{} with breakage', '{} with small scratches',
            '{} with burnt', '{} with stuck together', '{} with spot'],
'chewinggum' : ['{} with corner missing', '{} with scratches',
            '{} with chunk of gum missing', '{} with colour spot', '{} with cracks'],
'fryum' : ['{} with breakage', '{} with scratches', '{} with burnt',
            '{} with fryum stuck together', '{} with colour spot'],
'macaroni1' : ['{} with color spot', '{} with small chip around edge',
            '{} with small scratches', '{} with breakage', '{} with cracks'],
'macaroni2' : ['{} with color spot', '{} with small chip around edge',
            '{} with small scratches', '{} with breakage', '{} with cracks'],
'pcb1' : ['{} with bent', '{} with scratch', '{} with missing', '{} with melt'],
'pcb2' : ['{} with bent', '{} with scratch', '{} with missing', '{} with melt'],
'pcb3' : ['{} with bent', '{} with scratch', '{} with missing', '{} with melt'],
'pcb4' : ['{} with scratch', '{} with extra', '{} with missing',
            '{} with wrong place', '{} with damage', '{} with burnt', '{} with dirt'],
'pipe_fryum' : ['{} with breakage', '{} with small scratches', '{} with burnt',
            '{} with stuck together', '{} with colour spot', '{} with cracks']

```

Figure 6. Manual anomaly suffixes used to instantiate class-conditional prompts.

specific cues and evolves during training, its semantics may fluctuate across samples; the fixed prefix constrains the prompt space to consistent anomaly-related concepts (e.g., normality vs. abnormality), which stabilizes optimization and mitigates semantic drift. At the shallow input layer, the `encode_text_with_prefix` function (defined in `VVCLIP.py`) assembles all components via direct concatenation and pads the sequence to the maximum context length $L_{\text{ctx}} = 77$. The resulting order is:

$$[\text{SOT}] \rightarrow p_{\text{def}}^{\text{shallow}} \rightarrow p_{\text{prefix}} \rightarrow [\text{EOT}] \rightarrow [\text{PAD}].$$

In contrast, deeper layers ($i > 0$) adopt a replacement strategy rather than concatenation. Within each `ResidualAttentionBlock`, the prompt tokens from the previous layer are removed and substituted with the cur-

rent deep prompt $p_{\text{def}}^{\text{deep}(i)}$. The resulting sequence becomes:

$$[\text{SOT}] \rightarrow p_{\text{def}}^{\text{deep}(i)} \rightarrow p_{\text{prefix}} \rightarrow [\text{EOT}] \rightarrow [\text{PAD}].$$

This replacement preserves the original sequence length and positional alignment while allowing hierarchical DCF guidance to influence intermediate representations.

Additional Loss Design Details. Our unified training framework is guided by a Concept-Boundary Loss (CBL), \mathcal{L}_{CBL} , consisting of:

$$\mathcal{L}_{\text{CBL}} = \lambda_{\text{abf}} \mathcal{L}_{\text{ABF}} + \lambda_{\text{psg}} \mathcal{L}_{\text{PSG}} + \lambda_{\text{seg}} \mathcal{L}_{\text{SEG}}. \quad (13)$$

Pixel-level Segmentation Loss (\mathcal{L}_{SEG}). This auxiliary loss provides spatial supervision on synthetic anomalies

generated via cut-and-paste [10]. It combines:

$$\mathcal{L}_{SEG} = \mathcal{L}_{Focal} + \mathcal{L}_{Dice}. \quad (14)$$

Prompt Semantic Grounding Loss (\mathcal{L}_{PSG}). It ensures that the dynamically generated “normal” and “abnormal” prompts remain semantically stable and visually grounded. It consists of two components:

$$\mathcal{L}_{PSG} = \mathcal{L}_{text} + \mathcal{L}_{fg}. \quad (15)$$

The first component provides coarse-level semantic stabilization. It aligns the final [EOS] embeddings of the dynamic prompts (p_q^+ and p_q^-) with manually defined textual anchors (p_{man}^+ and p_{man}^-), ensuring that the semantic meaning of the prompts remains consistent throughout training:

$$\begin{aligned} \mathcal{L}_{text} = \frac{1}{4} & \left[(1 - \text{sim}(p_q^+, p_{man}^+)) + (1 - \text{sim}(p_q^-, p_{man}^-)) \right. \\ & \left. + \text{sim}(p_q^-, p_{man}^+) + \text{sim}(p_q^+, p_{man}^-) \right]. \end{aligned} \quad (16)$$

The second component performs fine-grained grounding at the token level. Using prompt tokens T and visual patch features V , it computes token-to-patch attention [2]:

$$W_{att} = \text{Softmax}(TV^\top), \quad V_{grp} = W_{att}V, \quad (17)$$

and constructs similarity matrices:

$$S_{ti} = TV_{grp}^\top, \quad S_{it} = V_{grp}T^\top. \quad (18)$$

The final fine-grained grounding loss is a symmetric cross-entropy objective:

$$\begin{aligned} \mathcal{L}_{fg} = \frac{1}{4N} \sum_{i=1}^N & \left[\text{CE}(S_{ti}^+, I) + \text{CE}(S_{it}^+, I) + \text{CE} \right. \\ & \left. (S_{ti}^-, I) + \text{CE}(S_{it}^-, I) \right]. \end{aligned} \quad (19)$$

B. Additional Ablation and Experiments

Finetune Layers. We evaluate the effect of the number of LoRA-finetuned top layers (L_v) in the visual encoder, with the results summarized in Table 8. The framework remains competitive even with a fully frozen encoder ($L_v = 0$), but finetuning the upper layers consistently yields moderate improvements. The best performance is achieved at $L_v = 12$ on MVTec-AD and $L_v = 8$ on VisA, which aligns with the settings adopted in our main experiments.

DCF Depth. Table 9 reports the influence of the depth of the Dynamic Concept Fusion (DCF) module. A depth of 1, which effectively removes deep prompt modeling, yields the weakest performance. Increasing the depth steadily strengthens results, demonstrating the value of hierarchical

Finetune Layers	MVTec-AD		VisA	
	AUROC _I	AUROC _P	AUROC _I	AUROC _P
0	94.6	96.0	86.9	97.3
6	94.7	96.1	86.6	97.4
8	94.2	95.9	87.3	97.4
12	94.8	96.2	86.3	97.4
14	94.8	96.2	86.7	97.4

Table 8. Ablation on the number of LoRA-finetuned top layers of the visual encoder under the 1-shot setting.

DCF Depth	MVTec-AD		VisA	
	AUROC _I	AUROC _P	AUROC _I	AUROC _P
1	94.2	95.9	86.2	97.3
3	94.2	95.8	86.0	97.3
5	94.7	95.9	86.7	97.4
6	94.7	96.0	87.0	97.4
7	94.8	96.2	87.3	97.4
8	94.5	96.1	87.3	97.4

Table 9. Ablation of DCF module depth under the 1-shot setting.

\mathcal{L}_{ABF}	\mathcal{L}_{SEG}	\mathcal{L}_{PSG}	MVTec-AD		VisA	
			AUROC _I	AUROC _P	AUROC _I	AUROC _P
✗	✗	✗	91.1	95.0	81.9	95.6
✓	✗	✗	92.2	95.5	82.3	96.1
✗	✓	✗	92.5	95.3	84.7	96.2
✗	✗	✓	92.6	95.1	82.0	96.0
✗	✓	✓	92.7	95.3	84.9	96.2
✓	✗	✓	94.6	95.9	82.5	96.6
✓	✓	✗	94.6	96.1	86.9	97.4
✓	✓	✓	94.8	96.2	87.3	97.4

Table 10. Ablation of the Loss Functions under the 1-shot setting. “✓” indicates inclusion; “✗” indicates exclusion.

Resolution	MVTec-AD		VisA	
	AUROC _I	AUROC _P	AUROC _I	AUROC _P
224px	94.8	96.2	87.3	97.4
336px	96.0	96.4	88.3	97.7

Table 11. Precision differences between 224px and 336px resolutions under the 1-shot setting. The 224px setting is maintained for fair comparison with previous methods.

textual guidance. Both datasets reach peak performance at depth 7, confirming the architectural choice used throughout the main experiments.

Loss Functions. Table 10 presents a detailed ablation of the three components of our Concept-Boundary Loss (CBL).

The results clearly substantiate the role of each term and how their interaction contributes to the formation of a reliable anomaly boundary.

We first examine the behavior of the model when individual loss components are removed. A model trained without any of the losses (Row 1) effectively collapses into a weak baseline that relies only on the pretrained visual-text alignment. Introducing \mathcal{L}_{ABF} alone (Row 2) already improves performance, demonstrating that driving an explicit adversarial search around the boundary meaningfully strengthens the decision function. However, this improvement is limited: without spatial constraints or semantic regularization, the crafted adversarial features do not fully align with true anomaly characteristics, and the resulting boundary lacks coherence.

Removing \mathcal{L}_{ABF} but retaining the auxiliary losses (Rows 3–5) yields slightly stronger performance than using \mathcal{L}_{ABF} alone. This indicates that \mathcal{L}_{SEG} and \mathcal{L}_{PSG} contribute complementary forms of guidance. \mathcal{L}_{SEG} encourages the model to maintain spatial sensitivity and prevents the text embeddings from drifting away from localized visual evidence. Meanwhile, \mathcal{L}_{PSG} regularizes the semantic space, ensuring that text prompts maintain meaningful contrast between normal and abnormal concepts.

Still, without \mathcal{L}_{ABF} , the model lacks the mechanism needed to precisely sculpt the decision boundary itself, leading to noticeably weaker AUROC. Rows 6 and 7 reveal the effect of pairing \mathcal{L}_{ABF} with only one auxiliary loss. The combination with \mathcal{L}_{PSG} (Row 6) improves semantic discrimination but remains limited by the lack of spatial grounding. Conversely, pairing with \mathcal{L}_{SEG} (Row 7) significantly strengthens spatial alignment and yields strong performance on both datasets, suggesting that guiding the forged boundary with pixel-level cues is especially beneficial for fine-grained anomaly localization.

The full model (Row 8), which incorporates all three components, achieves the best overall performance. This confirms that \mathcal{L}_{ABF} serves as the core driver of boundary formation, while \mathcal{L}_{SEG} and \mathcal{L}_{PSG} act as essential stabilizers that anchor the forged boundary to both spatial and semantic structures. The synergy of the three losses yields a boundary that is not only sharp but also consistent and interpretable, and this combination is crucial for achieving state-of-the-art results.

visual bank	text bank	MVTec-AD		VisA	
		AUROC _I	AUROC _P	AUROC _I	AUROC _P
✗	✗	88.9	92.7	78.7	94.9
✓	✗	94.5	96.0	87.1	97.2
✓	✓	94.8	96.2	87.3	97.4

Table 12. Ablation of visual bank and text bank under the 1-shot setting. “✓” indicates inclusion; “✗” indicates exclusion.

Resolution Ablation. Table 11 demonstrates the precision differences between 224px and 336px resolutions under the 1-shot setting. We keep the 224px resolution for consistency with previous work [12]. The results indicate that increasing the resolution to 336px slightly improves performance, as evidenced by higher AUROC scores on both MVTec-AD and VisA datasets.

Ablation on visual and text banks. We conduct an ablation study to examine the influence of the visual bank and the text bank on anomaly detection performance. As shown in Table 12, disabling both banks results in the weakest performance on MVTec-AD and VisA, underscoring the need for external reference structures in our framework. Our model’s core mechanism hinges on loss-driven boundary formation: the Adversarial Boundary Forging (ABF) loss explicitly generates adversarial features near the boundary between normal and abnormal classes, while the Segmentation and Prompt Semantic Grounding (PSG) losses anchor the boundary to spatial and semantic structures respectively. Within this paradigm, enabling the visual bank alone yields a substantial performance improvement because the visual prototypes provide rich reference points around which the boundary can be forged and stabilized in the visual feature manifold. When the text bank is added, only modest further gains are observed, since the global text embeddings already deliver strong semantic anchors through PSG and ABF. In this sense, the text bank acts as an auxiliary refinement layer in the loss-guided boundary shaping process rather than a primary driver. Therefore, the visual bank remains the dominant contributor in constructing a clear, robust boundary under our multi-class framework, while the text bank offers complementary textual information that gently refines the decision frontier.

C. More Visualization Results

Qualitative comparison with prior methods.. Figure 7 provides a detailed qualitative comparison between ABounD and recent few-shot anomaly detection methods, including PromptAD and IIPAD, across representative categories from both MVTec-AD and VisA. Overall, ABounD produces anomaly maps that are not only sharper but also substantially more spatially coherent. On texture-type categories such as *Carpet*, *Tile*, and *Grid*, prior methods frequently activate large background areas or generate scattered noise that does not correlate with the defect patterns, whereas ABounD generates compact responses that align closely with the ground-truth abnormal regions. For object-type classes including *Capsule*, *Cable*, and *Pill*, PromptAD and IIPAD often struggle with either overactivation around normal structures or blurred boundaries between normal

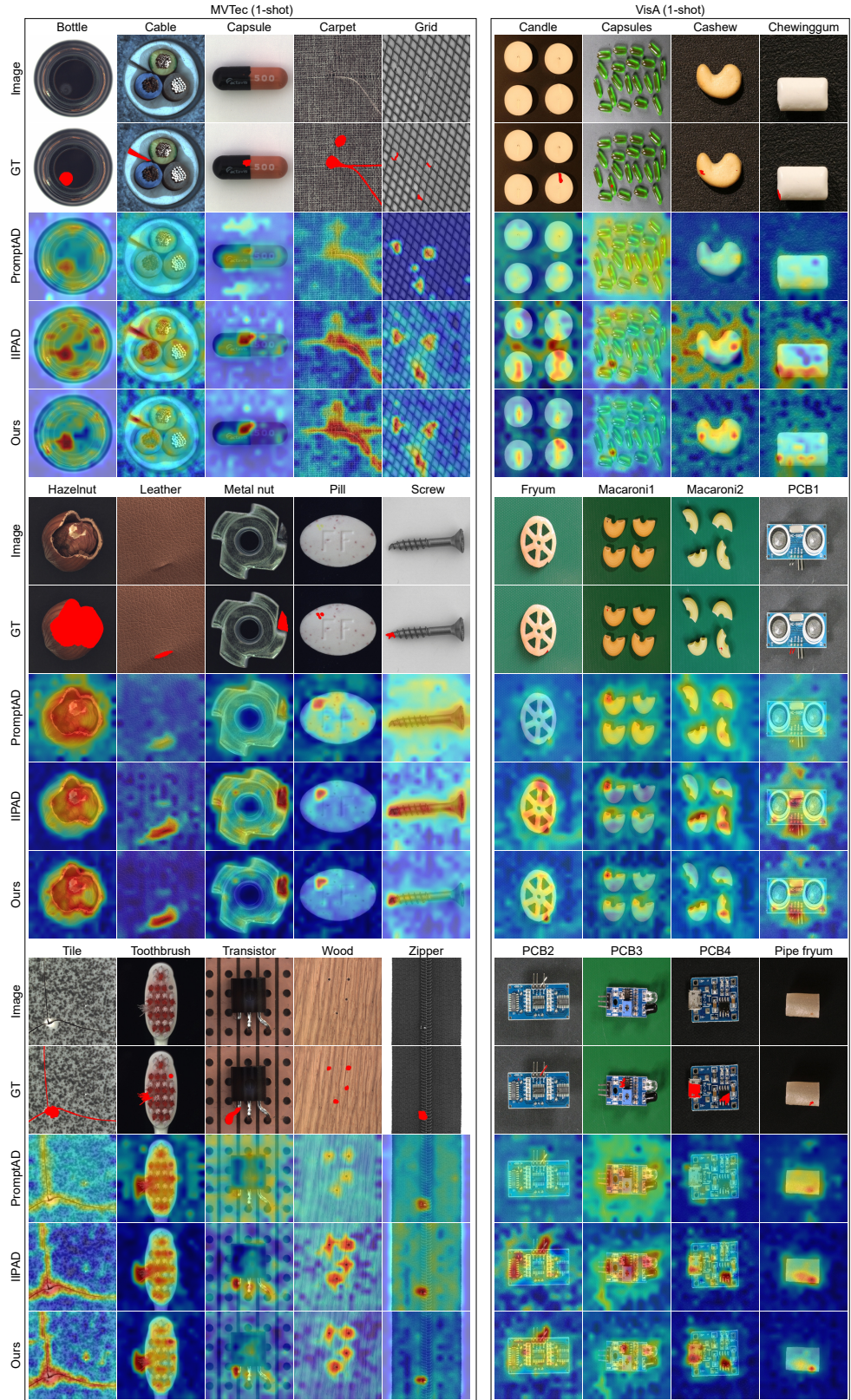


Figure 7. Qualitative visualization of anomaly localization results on MVtec-AD and VisA under the 1-shot setting. Compared methods include PromptAD, IIPAD, and our ABounD.

and abnormal areas, especially when the object surface is cluttered or contains repetitive microstructures. In contrast, ABounD suppresses such artifacts effectively and focuses its activation primarily on the true structural inconsistencies or fine appearance deviations. This improvement is consistent across both datasets, reflecting the advantage of our boundary-forging mechanism in aligning the learned decision surface with high-frequency, defect-relevant cues instead of being distracted by nuisance variations in illumination, clutter, or manufacturing patterns.

Fine-grained anomaly localization. Figure 8 highlights the behavior of ABounD on three VisA categories—Capsule, PCB1, and Pipe fryum—where anomalies are extremely small, distributed, or embedded within highly structured backgrounds. In the *Capsule* examples, defects typically manifest as tiny dents, scratches, or faint surface irregularities. These defects are difficult to capture because they often blend into the natural illumination gradients produced by the glossy capsule surface. Nevertheless, ABounD produces highly concentrated heatmaps around the small defective regions while keeping the remaining capsules inactive, demonstrating its ability to separate true defects from lighting-induced variations. In the *PCB1* case, anomalies involve missing or shifted components within a visually complex printed circuit board layout, where numerous edges and repeated patterns tend to confuse most methods. ABounD is able to localize these structural breaks with high precision, avoiding the background circuitry and primarily attending to the anomalous modules. For *Pipe fryum*, anomalies correspond to subtle deformations in thin, semi-transparent ring-shaped food items. Despite the low contrast between the rings and the green background, our method detects the small structural irregularities while avoiding overactivation on normal samples. These examples illustrate that ABounD maintains robustness in fine-grained detection scenarios and successfully exploits the boundary information forged by our multi-stage loss design to capture subtle, localized deviations.

Failure cases in the multi-class 1-shot setting. As shown in Fig. 9, several failure cases arise when anomalies lie extremely close to the normal appearance manifold induced by the multi-class 1-shot configuration. In the *Cable* and *Metal nut* categories, most anomalies take the form of color swaps, minor geometric flips, or rotations that preserve global object identity. Because the multi-class boundary is constructed from only a single normal instance per category, these transformations are interpreted by the pre-trained CLIP encoder—and subsequently by ABounD—as ordinary intra-class variations instead of abnormal patterns. Consequently, the predicted anomaly responses remain weak, causing under-detection. For *Capsules*, the anomalies correspond to tiny bubbles and faint surface dis-

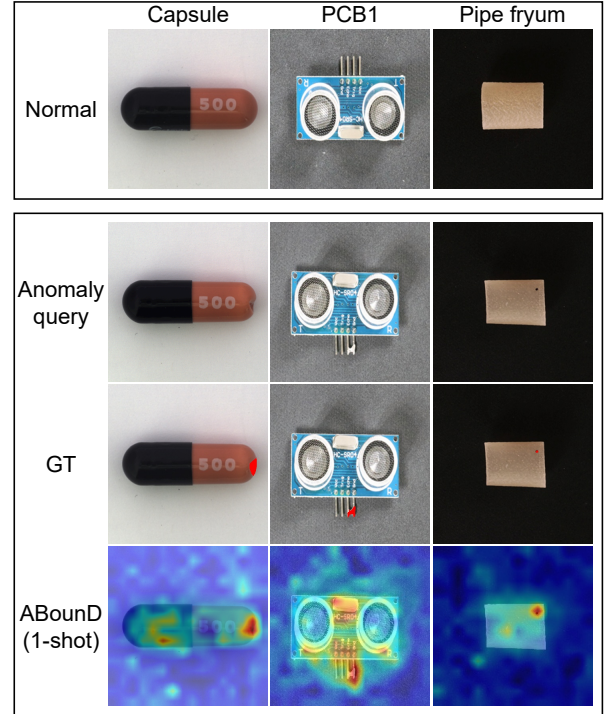


Figure 8. Qualitative visualization of anomaly localization results on MVtec-AD and VisA under the 1-shot setting. Compared methods include PromptAD, IIPAD, and our ABounD.

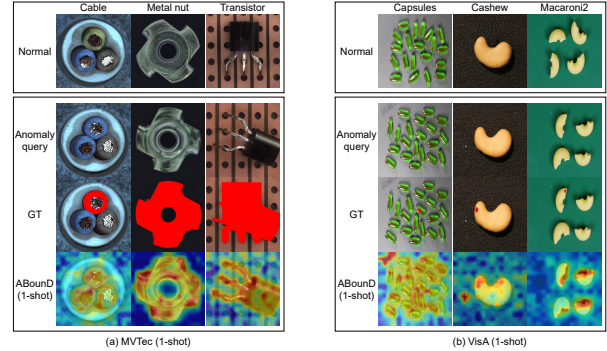


Figure 9. Representative failure cases of ABounD under the 1-shot setting on MVtec-AD and VisA. For each category, we show a normal support image, an anomalous query image, the ground-truth mask, and the anomaly map predicted by ABounD. These cases highlight the difficulty of handling color/pose-preserving variants and extremely subtle low-contrast defects from only a single normal exemplar.

tortions that appear under strong directional lighting. Their contrast relative to the background material is extremely low, and their spatial distribution is sparse, so the anomaly signal is easily overshadowed by illumination-induced gradients that dominate the embedding space. In *Transistor*, the anomaly primarily results from an unusual spatial lay-

out: the transistor is placed in an irregular position on the board. However, with only one normal support image, the model cannot infer any positional prior, and thus remains insensitive to such layout violations. For *Cashew* and *Macaroni2*, the anomalies involve extremely small contrast variations around the boundary of the object. Since the differences from the normal appearance are subtle and distributed across smooth curves, the forged boundary tends to favor coarse semantic cues and overlooks these local deviations. Taken together, these failures highlight a structural limitation of multiclass 1-shot learning: coarse class-level semantics dominate boundary formation in the absence of sufficient intra-class diversity, reducing the system’s sensitivity to color perturbations, pose-preserving changes, illumination effects, and other fine-grained defect signatures.

D. Detailed Comparison Results

To dissect our model’s performance in greater detail, we provide extensive experimental results for each subclass within the MVTec-AD and VisA datasets.

MVTec-AD Dataset. Tables 13 and 14 report the image-level and pixel-level AUROC (Area Under the Receiver Operating Characteristic curve) and AUPR (Area Under the Precision-Recall curve) scores of ABounD and the baselines on each MVTec-AD category under the 1-shot, 2-shot, and 4-shot settings. Across almost all object and texture classes, ABounD consistently attains the highest or near-highest AUROC and AUPR scores, with the gains being particularly pronounced on challenging categories such as *Cable*, *Capsule*, *Grid*, and *Screw*, where traditional feature-matching methods struggle with strong intra-class variation and cluttered backgrounds. Moreover, the standard deviations of ABounD across different few-shot trials remain relatively small compared to prior methods, indicating that the proposed boundary-forging mechanism yields a more stable decision function under multi-class few-shot sampling. Taken together, the per-category statistics confirm that ABounD not only improves the mean performance on MVTec-AD but also delivers robust behavior across diverse defect types and varying numbers of support images.

VisA Dataset. For the more structurally diverse and challenging VisA dataset, Tables 15 and 16 summarize the image-level and pixel-level AUROC and AUPR scores for each category. ABounD achieves consistently strong performance across both food-like textures (e.g., *Fryum*, *Pipefryum*, *Cashew*) and highly structured electronic boards (e.g., *PCB1*), where anomalies often manifest as subtle local defects or fine-grained structural changes. Compared with SPADE, WinCLIP, PromptAD, and IIPAD, our method not only yields higher average AUROC and AUPR scores in all few-shot regimes, but also exhibits reduced variability across different shots and categories, suggesting that the

forged multi-class boundary is less sensitive to the particular choice of support examples. These detailed results highlight that ABounD remains robust and high-precision in complex multi-class few-shot scenarios, where both intra-class appearance diversity and cross-class interference are significant.

E. Limitation

Although ABounD exhibits strong robustness in the multi-class few-shot setting, several inherent limitations remain due to the structure of boundary forging and the restricted number of normal exemplars.

First, the adversarial boundary forged by PGD is fundamentally constrained by the representation provided by only a few support samples per category. While the ABF module enriches the decision frontier with locally adversarial features, the underlying normal manifold remains narrow when only limited examples are available. Consequently, defects that manifest as subtle, low-contrast, or sparsely distributed appearance changes—such as tiny surface bubbles, faint scratches, or minor geometric distortions—may lie too close to the few-shot normal manifold and thus be misclassified as normal. These errors reflect the fact that ABF can sharpen the boundary only around the observed exemplars rather than the full range of intra-class appearance variation.

Second, ABounD may misidentify certain normal samples as abnormal when they deviate too far from the few available prototypes in high-dimensional space. In multi-class few-shot learning, different categories often form clusters with uneven density. Normal samples that naturally exhibit larger intra-class variability—due to illumination changes, pose adjustments, or object diversity—can inadvertently fall closer to the forged abnormal region. Since ABF enforces maximal ambiguity at the estimated boundary, such distant-but-normal samples may be incorrectly flagged as anomalies.

Finally, because the PGD procedure explores only local neighborhoods around each support feature, the forged boundary does not fully capture long-range or cross-category relationships in the CLIP embedding manifold. This limits ABounD’s ability to model anomaly types that depend on positional priors, object arrangement, or global structural relations that cannot be deduced from few support examples.

Together, these limitations highlight the fundamental difficulty of constructing a globally accurate anomaly boundary under few-shot constraints. Future work may consider expanding prototype diversity through synthetic augmentation, exploiting cross-category structure, or developing manifold-aware adversarial exploration strategies to reduce sensitivity to both subtle anomalies and naturally diverse normal patterns.

MVTEC Image-level	1-shot					2-shot					4-shot				
	SPADE	WinCLIP	PromptAD	IIPAD	ABounD	SPADE	WinCLIP	PromptAD	IIPAD	ABounD	SPADE	WinCLIP	PromptAD	IIPAD	ABounD
Bottle	81.6/94.0	98.9/99.7	98.5/99.9	99.3/99.7	99.7/99.9	94.3/98.1	99.2/99.8	98.5/99.4	99.8/99.9	99.9/100.0	88.0/96.0	99.2/99.8	96.3/98.0	99.1/99.5	99.9/100.0
Cable	34.8/65.8	78.0/87.1	83.5/91.6	92.4/95.9	92.2/95.7	34.9/65.8	83.9/90.6	85.7/92.2	92.1/95.7	93.9/96.4	35.7/65.2	82.3/90.0	86.0/91.9	95.4/97.3	93.7/96.4
Capsule	46.5/76.1	75.5/93.9	64.1/86.1	80.1/95.2	91.9/98.0	65.8/86.8	65.5/88.3	63.8/84.9	91.8/98.2	93.0/98.3	87.4/95.8	80.1/94.8	90.7/96.8	94.5/98.7	94.2/98.7
Carpet	72.3/87.2	99.9/100.0	99.9/100.0	99.6/99.8	100.0/100.0	87.0/95.0	99.9/100.0	98.5/99.4	100.0/99.9	100.0/100.0	92.5/97.4	99.9/100.0	97.3/98.3	100.0/99.8	100.0/100.0
Grid	91.0/97.1	99.6/99.9	98.7/99.8	96.6/98.8	98.9/99.7	94.4/98.3	99.2/99.7	95.9/98.5	97.0/98.9	99.1/99.7	97.2/99.2	99.5/99.8	97.3/98.3	96.0/98.4	99.4/99.8
Hazelnut	49.0/80.9	94.9/97.4	98.3/99.4	97.6/99.0	99.9/100.0	85.3/94.4	95.2/97.5	98.3/99.3	98.5/99.3	99.9/99.9	92.9/97.7	94.7/97.2	96.3/97.7	98.5/99.2	99.8/99.9
Leather	61.1/74.4	100.0/100.0	99.9/100.0	99.6/99.8	100.0/100.0	66.2/76.7	100.0/100.0	98.5/99.4	100.0/99.9	99.7/99.8	74.7/83.7	100.0/100.0	97.3/98.3	100.0/99.8	99.9/100.0
Metal nut	62.2/89.7	98.0/99.6	97.5/99.6	99.0/99.7	99.5/99.9	70.0/91.9	97.8/99.5	94.7/97.7	99.7/99.8	99.5/99.9	75.5/93.7	98.9/99.8	97.3/98.3	99.9/99.8	99.6/99.9
Pill	51.8/61.5	88.9/97.6	87.8/97.2	96.2/99.2	97.8/99.6	60.7/71.4	91.8/98.3	87.6/96.5	98.8/99.8	97.4/98.7	87.0/92.4	98.7/96.0	96.6/99.2	97.2/99.5	97.2/99.5
Screw	42.4/83.2	85.1/95.1	73.9/91.6	76.4/86.8	75.3/90.6	48.4/85.0	82.7/93.3	79.7/92.9	81.5/92.5	81.0/92.9	54.8/86.6	84.4/94.0	81.5/92.0	82.1/91.8	81.4/92.9
Tile	53.7/88.1	100.0/100.0	99.7/100.0	99.3/99.7	98.2/99.3	55.8/88.4	100.0/100.0	97.8/99.1	99.5/99.7	99.7/99.9	69.8/92.4	100.0/100.0	96.5/97.9	99.9/99.7	99.7/99.9
Toothbrush	44.0/72.2	94.2/97.7	94.3/98.1	91.5/97.1	98.7/99.5	44.6/70.6	93.9/97.6	98.5/99.4	92.5/97.4	98.8/99.6	49.0/72.9	98.1/99.3	96.1/97.8	92.5/97.3	99.3/99.8
Transistor	55.0/81.1	85.5/80.8	73.6/62.6	91.0/89.6	90.1/85.4	55.8/73.2	85.4/81.0	85.7/76.6	90.4/88.2	92.0/88.2	56.5/93.5	85.6/82.6	91.7/90.5	91.2/89.0	92.1/87.4
Wood	68.8/64.5	98.7/99.6	98.5/99.8	99.0/99.6	99.2/99.8	74.3/70.4	98.9/99.7	97.4/99.0	99.2/99.7	99.5/99.8	79.4/75.6	98.9/99.7	96.5/98.0	99.6/99.7	99.0/99.7
Zipper	67.3/89.3	94.9/98.6	95.2/99.1	89.0/95.4	79.7/94.0	88.7/96.9	97.2/99.2	92.0/97.6	95.5/98.6	98.2/99.5	92.3/98.0	97.0/99.2	93.1/97.2	96.0/98.6	98.8/99.7
Mean	58.8/80.3	92.8/96.5	90.9/95.0	93.8/97.0	94.8/97.5	68.4/84.2	92.7/96.3	91.5/95.5	95.6/97.8	96.8/98.2	76.6/88.8	94.0/96.9	93.4/96.5	96.1/97.9	97.0/98.3

Table 13. Comparison of image-level anomaly detection in terms of AUROC and AUPR on MVTEC.

MVTEC Pixel-level	1-shot					2-shot					4-shot				
	SPADE	WinCLIP	PromptAD	IIPAD	ABounD	SPADE	WinCLIP	PromptAD	IIPAD	ABounD	SPADE	WinCLIP	PromptAD	IIPAD	ABounD
Bottle	66.9/58.9	95.1/94.5	94.6/87.3	97.7/94.8	98.0/95.1	67.3/60.6	95.5/85.8	95.1/90.1	98.1/95.2	98.1/95.0	67.5/61.5	95.2/84.8	95.7/91.4	98.0/95.1	98.1/95.0
Cable	57.2/30.7	74.6/55.9	76.9/73.6	94.2/86.6	94.1/88.2	58.1/34.6	76.4/62.1	79.9/74.7	94.8/89.5	94.8/88.5	60.2/35.3	77.1/61.5	82.5/78.8	95.8/90.8	95.4/89.3
Capsule	61.7/51.4	95.6/89.0	94.7/87.4	96.5/91.2	96.6/92.2	62.5/52.3	94.7/84.2	94.0/88.5	97.0/92.6	96.8/92.4	63.8/51.7	96.3/88.9	96.5/88.7	96.6/88.5	97.4/93.6
Carpet	63.1/56.3	99.1/96.4	99.2/95.0	98.8/98.0	99.5/98.1	62.3/55.8	99.1/96.1	98.4/95.4	99.0/98.0	99.5/98.2	61.8/57.9	99.1/96.0	98.0/94.6	98.9/97.3	99.5/98.2
Grid	64.7/59.7	95.1/85.3	96.9/90.1	95.9/88.3	98.2/92.4	66.9/60.9	96.3/88.1	95.2/87.7	98.4/93.3	97.6/62.1	96.0/86.8	95.6/89.9	97.5/90.9	98.5/93.7	98.5/93.7
Hazelnut	56.0/47.6	98.6/92.5	97.0/89.1	97.7/93.7	98.4/94.3	58.1/55.6	98.7/93.1	97.2/92.1	98.2/94.6	98.5/94.4	60.3/54.4	98.7/92.4	96.9/91.3	98.2/95.4	98.6/95.4
Leather	65.1/61.2	99.3/98.2	99.4/96.5	98.7/98.6	99.5/98.9	63.7/60.7	99.3/98.3	98.6/97.3	98.8/98.5	99.3/98.6	65.4/61.9	99.4/98.2	98.2/95.8	98.9/98.2	99.4/98.5
Metal nut	64.9/54.6	77.9/77.0	94.3/88.3	93.7/91.7	92.2/90.9	65.1/57.8	76.1/75.6	94.0/89.2	94.9/92.3	92.8/91.5	65.8/59.9	79.5/79.5	92.0/87.8	94.2/93.0	94.0/92.9
Pill	83.9/68.5	93.9/88.9	92.4/88.3	95.9/94.7	95.1/96.0	83.4/66.1	94.1/89.6	93.5/91.8	96.5/94.1	94.9/96.3	83.5/65.3	94.4/89.9	94.1/92.6	96.3/95.2	94.9/96.2
Screw	51.0/49.8	96.7/87.0	95.8/85.1	95.3/85.2	96.8/87.3	52.7/50.9	97.0/88.1	95.4/86.0	96.0/85.8	97.8/90.3	52.9/51.2	96.5/86.6	96.0/88.1	96.3/87.1	98.1/91.3
Tile	65.1/55.1	92.2/78.7	94.4/88.0	96.2/90.3	96.8/91.1	64.6/54.7	92.6/79.7	94.7/89.2	96.6/90.7	97.0/91.8	66.7/54.6	92.2/78.2	94.7/89.4	96.7/90.8	97.1/91.5
Toothbrush	55.9/53.7	95.1/86.5	99.1/91.6	96.7/82.3	98.2/89.0	57.2/57.2	84.5/85.6	98.4/91.6	96.9/82.9	98.4/89.4	57.3/59.1	96.8/88.5	98.0/90.3	97.3/84.0	98.3/90.4
Transistor	58.5/41.9	85.1/63.5	75.6/57.6	85.9/67.3	84.8/66.7	58.9/43.5	95.3/62.8	83.6/64.5	87.9/68.6	86.8/68.7	59.1/45.3	84.4/62.6	86.3/67.4	89.0/70.8	86.9/68.2
Wood	51.0/56.7	94.7/86.9	95.9/91.0	96.3/94.1	97.6/95.0	52.3/58.7	94.7/87.8	94.5/91.9	96.9/84.6	97.5/95.0	55.6/59.5	94.6/88.3	94.4/91.1	96.8/94.3	97.5/95.0
Zipper	41.0/50.2	92.9/81.9	97.7/90.7	95.3/88.2	96.6/90.5	42.4/51.7	92.4/81.8	96.5/90.2	96.2/89.6	98.2/94.6	46.7/54.2	92.9/83.0	95.7/89.2	96.1/90.4	98.4/95.2
Mean	60.4/53.1	92.4/83.5	93.6/87.3	95.7/89.7	96.2/91.1	61.2/54.7	92.4/83.9	93.9/88.0	96.2/90.3	96.6/91.9	62.8/55.6	92.9/84.4	94.3/88.4	96.4/90.8	96.9/92.3

Table 14. Comparison of pixel-level anomaly detection in terms of AUROC and PRO on MVTEC.

VisA Image-level	1-shot					2-shot					4-shot				
	SPADE	WinCLIP	PromptAD	IIPAD	ABounD	SPADE	WinCLIP	PromptAD	IIPAD	ABounD	SPADE	WinCLIP	PromptAD	IIPAD	ABounD
Candle	37.3/41.3	96.3/96.7	92.8/95.9	91.4/93.8	95.5/96.5	57.2/54.6	96.4/96.9	95.5/95.7	94.7/94.9	95.8/96.5	60.0/57.7	96.9/97.3	94.6/94.5	95.4/95.5	95.5/96.2
Capsules	51.8/65.6	79.3/87.0	89.2/95.2	88.4/94.4	92.5/96.0	56.6/68.8	81.6/89.1	85.9/93.7	89.5/94.5	90.2/94.3	60.1/71.9	83.0/90.0	85.4/91.6	90.0/96.0	86.3/92.9
Cashew	64.0/79.4	93.9/97.4	89.9/96.2	85.1/95.4	94.6/97.7	65.1/80.2	92.6/96.7	89.8/95.7	85.9/94.8	96.7/98.5	80.2/88.2	92.6/96.8	88.7/95.4	90.7/96.0	97.3/98.8
Chewinggum	67.5/83.6	97.9/99.1	96.5/98.1	97.2/98.8	97.2/98.8	74.5/87.2	98.1/99.2	97.3/98.8	97.0/98.8	96.9/98.8	86.6/93.0	98.4/99.3	96.8/98.9	97.5/99.3	97.0/98.8
Fryum	72.2/86.1	98.8/96.9	89.0/95.8	89.4/96.0	94.2/97.4	73.9/86.9	90.1/95.4	85.9/93.9	91.9/96.4	93.4/97.2	83.8/91.8	91.6/96.1	89.3/95.6	92.8/97.3	93.0/96.9
Macaroni1	65.1/63.5	81.9/82.8	87.3/88.9	84.8/89.0	95.8/90.5	59.5/56.1	86.4/87.2	87.6/92.0	83.9/90.3	90.9/92.8	59.2/55.5	86.9/87.4	87.8/90.8	87.9/91.2	91.4/93.1
Macaroni2	56.0/54.1	78.1/80.1	65.8/70.7	75.0/79.0	71.9/77.6	50.8/51.7	76.8/79.0	75.1/79.2	75.3/79.8	74.9/81.1	57.2/52.0	79.0/81.9	79.2/83.9	77.6/80.6	76.7/82.8
PCB1	73.4/73.2	83.8/83.7	84.0/76.5	83.0/77.1	89.1/89.7	78.2/77.7	85.5/84.1	83.1/79.0	85.7/78.1	93.6/93.9	84.1/84.6	86.0/85.6	84.8/81.6	84.7/78.6	91.2/91.4
PCB2	71.7/71.6	58.4/58.6	73.9/71.5	72.1/69.9	75.1/74.3	79.4/78.4	56.8/54.6	74.6/75.0	74.4/73.2	86.4/88.9	87.2/88.5	59.4/61.3	79.8/80.5	75.0/73.9	85.8/87.7
PCB3	58.5/58.6	64.9/66.2	70.9/69.8	71.3/72.9	69.7/71.5	63.7/62.1	67.7/67.3								